geosciences

MDPI

Article

The Magmatic Patterns Formed by the Interaction of the Hainan Mantle Plume and Lei–Qiong Crust Revealed through Seismic Ambient Noise Imaging

Mohan Pan [1,2], Ting Yang [2,3,*], Ba Manh Le [4], Yuhang Dai [5] and Han Xiao [6]

1 Harbin Institute of Technology, Harbin 150001, China; 11849522@mail.sustech.edu.cn
2 OBS Laboratory, Department of Ocean Science and Engineering, Southern University of Science and Technology, Shenzhen 518055, China
3 Shanghai Sheshan National Geophysical Observatory, Shanghai 201602, China
4 Institute of Geophysics (IGP), Vietnam Academy of Science and Technology (VAST), Hanoi 10072, Vietnam; manhle@igp.vast.vn
5 Ocean and Earth Science, National Oceanography Centre Southampton, University of Southampton, Southampton SO14 3ZH, UK; y.dai@soton.ac.uk
6 Helmholtz Center Potsdam, German GeoResearch Center GFZ, 14473 Potsdam, Germany; xiaohan@gfz-potsdam.de
* Correspondence: tyang@sustech.edu.cn; Tel.: +86-138-1880-7270

Abstract: Magmatism on continental lithospheres induced by mantle plumes is more complex compared to oceanic intraplate volcanism owing to the heterogeneous nature of continental crustal and lithospheric structures. Substantial evidence points to the deep-oriented Hainan mantle plume beneath the Lei–Qiong region, the southernmost of the South China block. In this study, we present a detailed shear wave velocity model of the crust and uppermost mantle in the Lei–Qiong volcanic region, derived from 3-year seismic data (2016–2018) from 34 stations and the use of the ambient noise tomography method. An evident columnar low-velocity anomaly was imaged in the crust and uppermost mantle beneath the Wushi Sag (WSS), Beibu Gulf, potentially suggesting that the center of either one branch or the entirety of the Hainan mantle plume impacts the crust here. This low-velocity anomaly is overlaid by a local Moho deepening, indicative of underplating beneath the existing crust. The Maanling–Leihuling Volcanic Field (MLVF) in northern Hainan Island, previously considered the center of the hotspot, does not exhibit such distinct velocity anomalies. Instead, subtle lower crustal anomalies beneath the MLVF are linked with the upper mantle low-velocity zone beneath the WSS. Additionally, the high-conductivity bodies beneath the MLVF indicate lateral magma transport. Earthquake swarms and deep-seated seismic events beneath the WSS further support the presence of magmatic processes. This study indicates that in the Lei–Qiong region, the interaction of the continental crust with the mantle plume centered in the WSS results in magma exhibiting both vertical ascent and lateral migration, leading to a dual low-velocity shear wave pattern in the upper crust, which significantly influences the surface volcanic activity.

Keywords: Hainan plume; crustal structure; intercontinental plume; ambient noise; surface wave

check for updates

Citation: Pan, M.; Yang, T.; Le, B.M.; Dai, Y.; Xiao, H. The Magmatic Patterns Formed by the Interaction of the Hainan Mantle Plume and Lei–Qiong Crust Revealed through Seismic Ambient Noise Imaging. *Geosciences* **2024**, *14*, 63. https://doi.org/10.3390/geosciences14030063

Academic Editors: Jesus Martinez-Frias, Lev V. Eppelbaum and Luciano Telesca

Received: 13 November 2023
Revised: 21 February 2024
Accepted: 21 February 2024
Published: 25 February 2024

1. Introduction

Hotspots, geological phenomena marked by concentrated volcanic activity, are found in various locations worldwide, with approximately 30% occurring within continents or along continental margins [1]. While oceanic hotspots are characterized by relatively straightforward interactions with thin and uniform oceanic lithospheres (e.g., [2]), continental hotspots, referring to hotspots located within continents or along continental margins, can give rise to more complex magmatism within the heterogeneous continental lithosphere [3,4]. These continental hotspots can manifest as multi-magma chambers, facilitate the migration of magma and hydrothermal fluids, or lead to magma pooling beneath thinned lithospheric sections [3,5–7]. Moreover, plume-driven magmatism and seismicity associated with continental hotspots can have significant environmental and societal impacts, contributing to metallogenesis and providing valuable insights into deep Earth dynamics [8]. Thus, the comprehensive investigation of the three-dimensional subsurface architecture surrounding continental hotspots is essential for accurately assessing volcanic hazards and resource potential.

In the southernmost regions of South China, encompassing the Leizhou Peninsula and Hainan Island (Figure 1), referred to as Lei–Qiong, extensive volcanic activities have been recorded across six phases since the Cenozoic era [9]. Late-Cenozoic alkali basalts are widely distributed in this region, covering more than 7200 square kilometers [10–12]. Notably, the most recent known eruption on Leizhou Peninsula and Hainan Island took place around 10,000 years ago at the Maanling–Leihuling Volcanic Field (MLVF) (Figure 1) [10,11]. Additionally, Weizhou Island and its twin, Xieyang Island, located west of Lei–Qiong in the eastern Beibu Gulf, represent the largest and youngest Quaternary volcanic oceanic islands in China [13,14]. Geologic and petrologic evidence suggests a major eruption on Weizhou Island approximately 6900 ± 100 years ago [15]. The Lei–Qiong region is one of the most seismically active areas in Chinese history (Figure 1) [16], with significant events such as the 7.5-magnitude Qiongshan earthquake [17] and the Beibu Gulf earthquakes of M_L 6.0 and 6.1 [18].

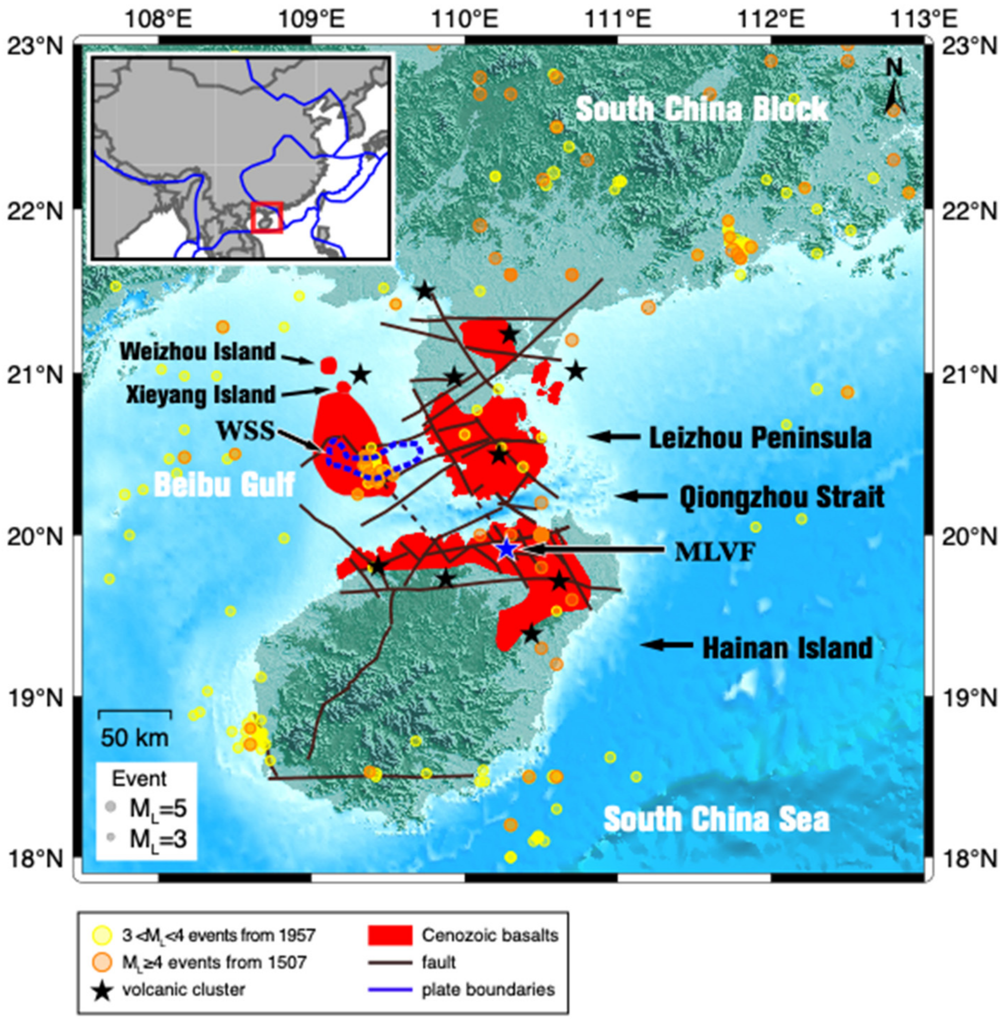

Figure 1. Map of the Lei–Qiong region showing its location with respect to regional tectonics (inset), major faults, volcanic clusters, and historical earthquakes in the region. The black dashed lines delineate

inferred seafloor faults, extending from those on land. The Cenozoic basalts coverage references the following two papers [16,19]. The stroked blue star indicates the Maanling–Leihuling Volcanic Field (MLVF) with the most recent volcanic activities. In addition, important geographical units are marked on the map, including the Wushi Sag (WSS) (blue dashed contour), Weizhou Island, and Xieyang Island. Here, we present earthquake data from two event lists with different start times and minimum earthquake magnitudes. We speculate that the reason for this difference is that due to technological limitations, before 1957, only earthquakes with a magnitude of 4 and above were recorded and preserved.

Tectonically, the Lei–Qiong area has been subjected to sustained compressional forces due to the Indian–Asian continental collision and the eastward subduction of the Philippine Sea plate [20]. Transitioning from an active to a passive continental margin since the late Cretaceous, the South China margin currently experiences minor NNW–SSE tension, accompanied by the preferential seaward extension of the lower crust [21–24]. In line with this regional extension, the Lei–Qiong area is characterized by NEE–SWW active faults, NNW–SSE faults, and E–W deep fracture zones (Figure 1) [10,25]. Notably, the crust's thickness varies, with the north exhibiting a thickness of about 30 km, gradually decreasing to around 27 km in the south, where the Moho also shallows considerably beyond the continental shelf and slope [26]. Comprehending how the crustal structure interacts with the deep-seated mantle plume and their magmatic pattern is crucial in understanding the region's present volcanic manifestation.

The existence of the Hainan plume was initially proposed through shear wave tomographic studies [27,28]. Subsequent geophysical and geochemical evidence strongly supports the idea that the Hainan plume, likely originating from the lower mantle, is responsible for the high-flux intraplate volcanism observed in this region. This has been substantiated by the identification of an abnormally thin mantle transition zone northeast of the Qiongzhou Strait through receiver functions and waveform modeling [19,29,30]. Moreover, body wave tomography offers direct insight into the morphology of the low-velocity conduit, revealing a slightly east-tilted plume stem beneath the mantle transition zone below the eastern Qiongzhou Strait [31–34]. At shallower depths, geochemical data provide further support, indicating that Quaternary volcanic products from local islets belong to alkali magma series and ocean island basalt (OIB)-incompatible elements, reflecting elevated mantle temperatures, pressures, and the presence of recycled oceanic crust component, thus corroborating the existence of an underlying plume [35].

While several geophysical studies have provided constraints on the near-surface structure (e.g., [13,36–40]), ongoing debate surrounds the nature of the interaction between the plume and the crust in the eastern Qiongzhou Strait and northernmost Hainan, referred to as the Hainan hotspot. Specifically, the mechanisms through which rising mantle materials interact with the crust, linking surface volcanism to deeper lithospheric processes, remain uncertain. Additionally, questions persist regarding whether this interaction has led to the uplifting or deepening of the Moho [19,38,41]. Although previous studies have carried out extensive imaging of the shallow lithosphere beneath the region [13,36–42], various limitations have hindered a comprehensive understanding. These limitations include focusing on excessively large study areas, emphasizing the deep lithosphere, or being confined to Hainan Island.

In this study, we constructed Rayleigh wave phase velocity maps and a 3D S-wave model spanning depths from 5 to 50 km across Lei–Qiong. We employed ambient noise tomography using data from both national and regional stations. Because we have included several stations in the southern coastal areas of Guangxi and Guangdong Province on the basis of the stations in the Lei–Qiong region, we enhanced resolution beneath both land and the east Beibu Gulf margin. Our study introduces a novel model that refines the location of the Hainan plume and its interaction with the crust, offering valuable insights into the magmatic pattern in this hotspot. Furthermore, the model of the Hainan plume has the potential to provide insights into other continental intraplate hotspots.

2. Materials and Methods

2.1. Data

The seismic data used in this study were collected from 34 permanent broadband stations spanning three provinces over a period of three years (Figure 2). Among these stations, a subset includes 23 densely arranged seismic stations located across Hainan Island, which continuously recorded data from January 2016 to September 2018. Additionally, there were four stations along the coast of Guangdong province operating from August 2018 to December 2018, and seven stations in Guangxi province, including two on Weizhou Island and Xieyang Island, recording data from September 2016 to December 2018. All stations were equipped with 3-component broadband seismographs, continuously sampling raw data at 100 Hz. The station aperture gradually decreases from north to south. More details about the stations can be found in Table A1.

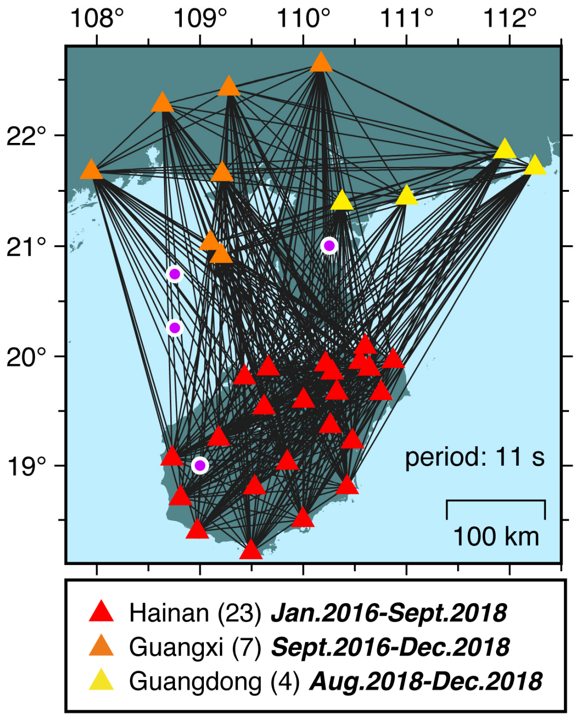

Figure 2. The distribution of the 34 seismic stations (triangles) used in this study and ray path coverages at the period of 11 s. Stations are color-coded by three administrative provinces of China, with station counts and seismic record durations listed in the legend.

2.2. Data Processing

We employed the data processing approach outlined by Bensen et al. [43] to derive ambient noise-normalized correlation functions (NCFs) for the station pairs. Daily continuous, vertical seismograms were down-sampled to 1 Hz and corrected for instrument responses. A total of 28,395 daily segments were utilized, averaging 835 segments per station. Subsequently, the seismograms underwent band-pass filtering, temporal normalization, and spectral whitening to eliminate the influence of earthquake signals. The NCFs for all station pairs were then computed and linearly stacked over the entire data period to enhance their Signal-to-Noise Ratios (SNRs) [43].

Figure 3 displays the NCFs aligned by interstation distance in the 5–10, 10–20, and 20–30 s period bands, where the Rayleigh wave signals are featured. The positive and negative lags of the NCFs correspond to signals traveling in opposite directions along the great circle path connecting the station pairs.

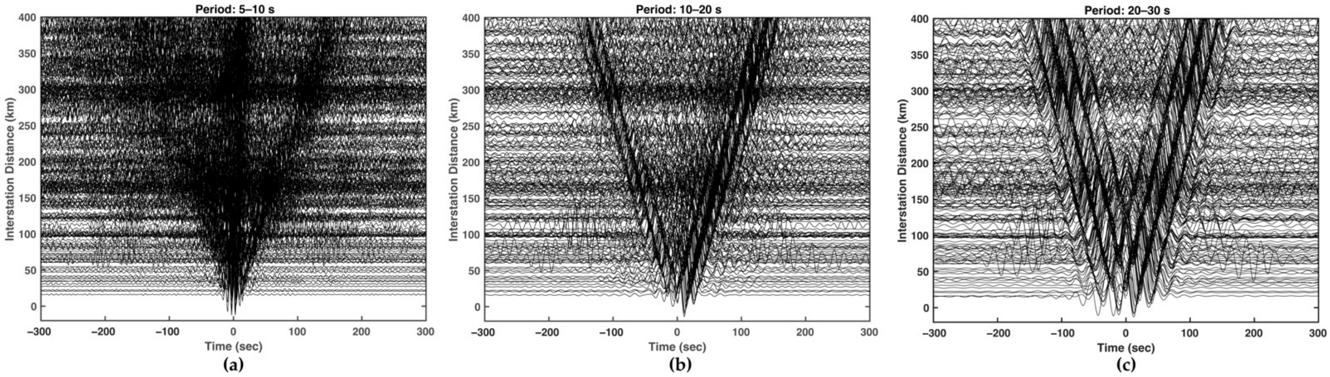

Figure 3. Normalized cross-correlation functions (NCFs) at periods of (**a**) 5–10 s, (**b**) 10–20 s, and (**c**) 20–30 s as a function of the interstation distance.

Due to the seasonal variations in the South China Sea (SCS)'s ocean state [44,45], the anisotropic nature of ambient noise energy in adjacent regions is evident [46,47] (see Figure S1 in the Supplementary Materials). These non-true-diffusive sources could introduce biases in the travel time of the causal or acausal sides of the NCFs, subsequently leading to errors in phase velocity inversion. However, prior investigations addressing this issue indicate that the travel time bias caused by undiffused noises is generally less than 1% (e.g., [48,49]). A similar study conducted in the SCS ocean basin utilizing OBS data reported a bias even smaller than 0.5% [50]. Nevertheless, we mitigated this effect by exclusively selecting NCFs with SNRs greater than 5.0 and averaging the causal and acausal sides of each NCF. Here, the SNR is defined as the ratio of the maximum amplitude of the envelope around a given frequency to the average amplitude of the envelope of a 150 s long noise segment immediately following the signal.

To extract phase velocity dispersion curves, we applied a semi-automated frequency–time analysis method to extract the phase velocity dispersion curves [51]. Given that the systematic error of the phase velocity inversion increases with the ratio of the wavelength to the station interval [51,52], we excluded NCFs with an interstation length less than two wavelengths. Finally, 450 phase velocity dispersion curves were obtained.

2.3. Phase Velocity Inversion

The phase velocity dispersions measured in each period were employed for the inversion of azimuthal isotropy phase velocity variations. The study region, spanning from 18° to 23° N and 107.5° to 112.5° E, was parameterized using a 21 × 21 node grid with 0.25° spacing. Despite our efforts to selectively choose high-quality dispersion curves and minimize the uneven distribution of noise sources, there remained the possibility of incorporating bad measurements and data outliers that could have introduced errors into the velocity model. Consequently, a two-step inversion was performed following the method outlined by Yao et al. [53]. In the initial step, all data with estimated measurement errors were included in the inversion with equal weighting. Subsequently, in the second step, data with residuals exceeding twice the standard deviation of all data residuals were assigned reduced weights, thereby decreasing their uncertainty [54].

More specifically, we utilized the continuous regionalization and generalized inversion scheme [53,55,56], as per Equation (1), to invert for the isotropic phase velocity, denoted as m.

$$\boldsymbol{m} = \boldsymbol{m}_0 + \boldsymbol{C}_m \boldsymbol{G}^T \left(\boldsymbol{G} \boldsymbol{C}_m \boldsymbol{G}^T + \boldsymbol{C}_d \right)^{-1} (\boldsymbol{d}_0 - \boldsymbol{G} \boldsymbol{m}_0) \tag{1}$$

where $\boldsymbol{d}_0$ is our observed data, $\boldsymbol{m}_0$ is the a priori model which is defined by the mean phase velocities within each frequency band, $\boldsymbol{G}$ is the sensitivity matrix, and $\boldsymbol{C}_d$ and $\boldsymbol{C}_m$ stand for the covariance matrix for the observed data and model.

Firstly, data with estimated measurement errors were used to perform inversion. The misfit between the derived and observed data was calculated. And in the later stage, the data with misfit greater than twice the standard deviation of all data residuals couple with a new larger uncertainty following Equation (2):

$$\hat{\sigma_d^i} = \sigma_d^i exp\left\{\frac{1}{2}\left(\frac{\varepsilon^i}{2\sigma} - 1\right)\right\} \quad (2)$$

where the $\hat{\sigma_d^i}$ is the new data uncertainty obtained by multiplying the original σ_d^i by a new exponent in which ε is the misfit and σ is the standard deviation of all data residuals.

The a priori model covariance function between the predicted model at two locations, r_1 and r_2, was determined as per Equation (3):

$$\boldsymbol{C}_m(r_1, r_2) = \sigma_s^2 exp\left(-\frac{(r_1 - r_2)^2}{2L^2}\right) \quad (3)$$

where σ_s represents the prior slowness uncertainty, and L is the correlation length of the model. The homogeneous starting model was the mean velocity in each period. We assigned the standard deviation as 8%, twice the estimated phase velocity measurements uncertainty, as suggested by Yao et al. [53]. The spatial correlation length is specified as 50 km, considering the ray path coverage (Figure 2) and synthetic resolution tests (Figure 4). From the equation, L plays the role of a spatial smoothing filter. L is assigned primarily based on ray coverage density and is, to some extent, subjective. Its value is also reflected in the final model's resolution, typically being twice the value of L [53–55].

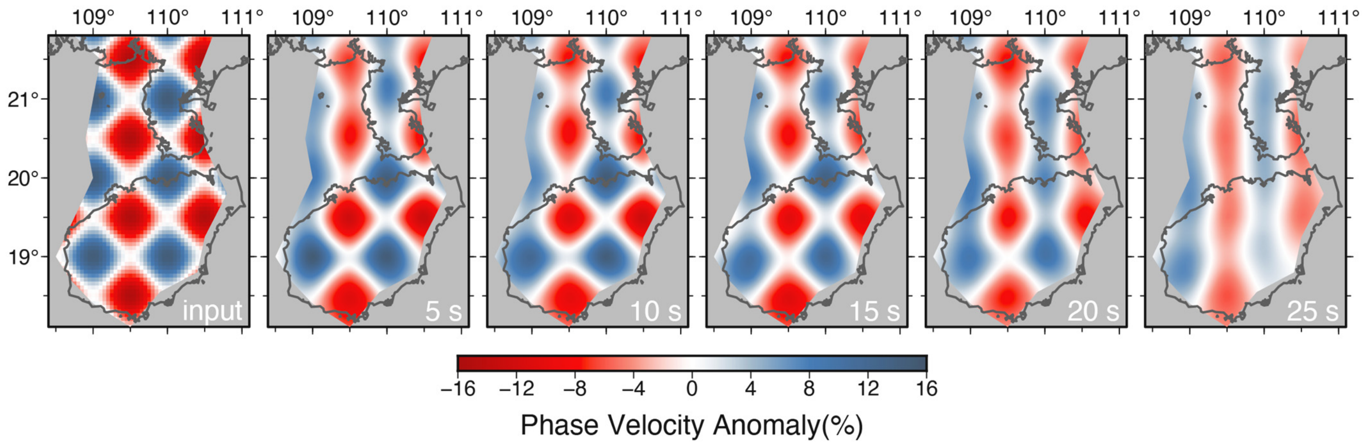

Figure 4. Checkerboard resolution test showing the input model and results at selected periods. The input synthetic models inherit the resolved mean velocity with ±15% perturbation, while the size of the anomaly is 0.7° × 0.7°.

2.4. Resolution Tests

To assess the dataset's resolving capabilities and interpret the resulting tomographic images, we conducted resolution tests. Checkerboard input models were employed in the first test, featuring alternating positive and negative 15% velocity perturbations relative to the mean at each period [57,58]. Additionally, a 1% random error was introduced to the synthetic phase velocity to simulate measurement errors [2]. Using identical parameters as the actual inversion, we recovered the anomaly patterns (Figure 4).

For periods shorter than 20 s, the input checkerboard patterns were generally well recovered across the majority of the Lei–Qiong area, with resolving capacities displaying significant variations for different periods. In the 5 to 20 s period range, characterized by relatively dense ray coverages (Figure S3 in Supplementary Materials), both the anomaly pattern and strength were accurately retrieved. However, noticeable smearing in the north–south direction was observed for periods exceeding 20 s, attributed to the elongated distribution of the stations. Additionally, there was a conspicuous reduction in the recovered strengths for these longer periods.

Following the same procedure as the checkerboard resolution test, we conducted inversions on the synthetic dataset and examined the recovery of the standalone anomaly (Figure 5). Despite the degradation in the resolving capacity with an increase in the periods and the noticeable smearing for longer periods, the detected anomalies were recovered fairly accurately across all periods, including those exceeding 25 s. The maximum strength remained relatively stable at around −14% for periods less than 25 s. The north–south smearing was deemed acceptable, with lateral smearing falling within satisfactory ranges of approximately 0.5° (half the input diameter) at 5 s and approximately 1° (the full input diameter) at 30 s.

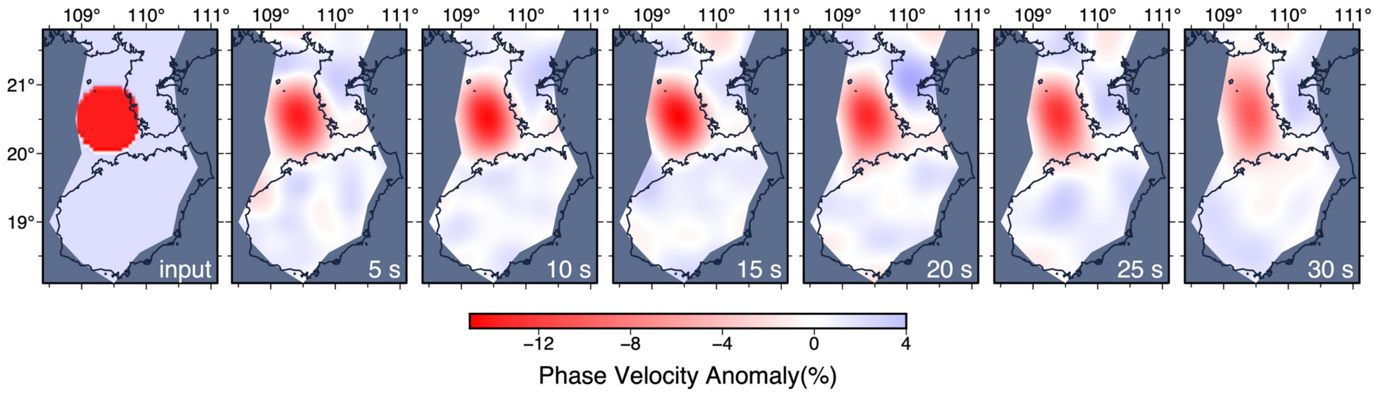

Figure 5. Synthetic resolution test for a standalone columnar low-velocity anomaly centered in the Wushi Sag (WSS) showing the input model and recovered anomaly at selected periods. The input model contains a −15% circular anomaly with a diameter of 1° at 20.5° N, 109.4° E.

Based on the results of the two resolution tests, these synthetic assessments demonstrate that, for periods less than 20 s—roughly aligning with the depths of the upper and middle crust (Figure 6b)—the dataset and inversion method proficiently recover anomalies with an effective dimension of 80 km. This encompasses the accurate detection of the anomaly's location and magnitude. However, as the periods increase, the resolution experiences a gradual degradation. For periods falling within the 20 to 30 s range, corresponding to the depth range of the lower crust and uppermost mantle (Figure 6b), the inversion process can only discern anomalies with dimensions of 120 km or larger, exhibiting a capacity that is marginally acceptable at best. This indicates a noticeable decline in the effectiveness of the data coverage and method as we delve into deeper layers.

2.5. Shear Wave Inversions

To derive a depth-dependent 3D shear wave velocity model from phase velocities, we initiated a 1D shear wave velocity inversion in the vertical direction at each grid point using phase velocities spanning 5 to 30 s. The resulting 1D models were subsequently combined and interpolated, forming a comprehensive 3D shear velocity structure for the Lei–Qiong region.

In the inversion process, we employed DISPER80 [59] to calculate partial derivatives of phase velocity with respect to shear velocity. Adopting a non-linear inversion method based on continuous models [55,56], we applied the damped least-squares inversion method [56] to update the phase velocities at each node, culminating in the development of the 1D S-wave velocity model. The inversion was executed iteratively until the decrease in misfit between the observed and calculated dispersion velocities reached a minimum. Figure 6a visually illustrates the comparison between the observed and final dispersion curves at four sites.

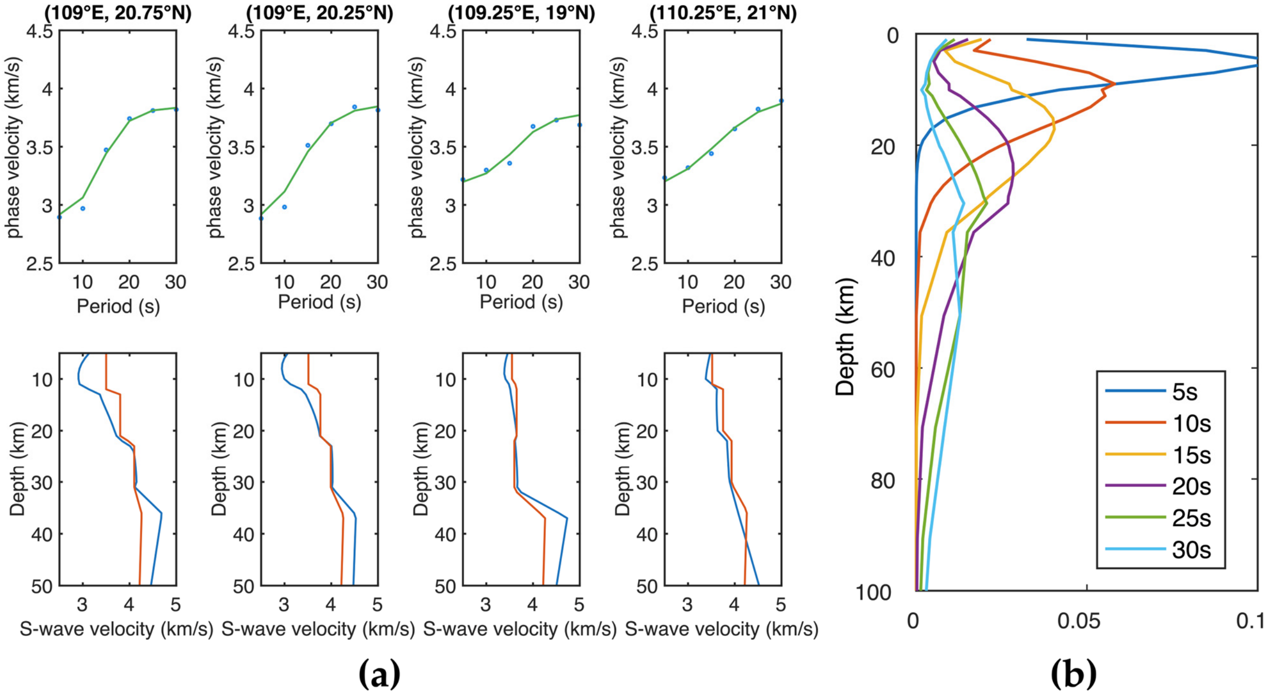

Figure 6. (**a**) Inversion results at four sites. The upper panels illustrate the comparison of the observed (blue dots) and the final (green lines) Rayleigh phase velocity dispersion curves. The lower panels show comparisons between the initial S-wave velocity model (red line) and the resultant model (blue line). The corresponding geographical coordinates are marked on top of the upper panels and depicted in Figure 2. (**b**) Normalized sensitivity kernels of Rayleigh waves at various periods, distinguished by different colors.

During the construction of the inverse objective function, we formulated a priori 1D starting models at each node, tailored based on their geographical locations. In this model, the crustal component was derived from the smoothed Crust 1.0 [60], and the mantle adhered to the laterally homogeneous IASP91 model (Figure 6a). Due to the relatively coarse lateral variations in the Crust 1.0 model, the initial velocity model for the crust at each node was computed by averaging the models of the surrounding eight nodes. It is important to note that, considering an average depth of ~17 m in the Qiongzhou Strait and Beibu Gulf based on the GEBCO bathymetric grid, the water layer was omitted from the starting model.

As depicted in Figure 6b, the sensitive depths of the 5–30 s Rayleigh waves fall within the range of 5–50 km. Consequently, our interpretation is specifically focused on structures within this depth range.

3. Results

3.1. Phase Velocity Structure

The tomography produced phase velocity anomalies within the period range of 5–30 s, with five periods shown in Figure 7. In line with the results of our resolution tests (Figures 4 and 5), our interpretations are focused on regions with robust ray coverage, while the remaining parameterized area is indicated in gray in the anomaly panels.

The phase velocity maps (Figure 7) reveal two prominent low-velocity anomalies at short periods of 5 and 10 s, which are particularly sensitive to the upper crust's structure. At 5 s, both anomalies exhibit a significant strength of approximately −15%. The first, a broader ellipse-shaped anomaly, is centered in the WSS, occupying a large portion of the eastern Beibu Gulf. The second anomaly is more localized, centered on the Qiongzhou Strait, encompassing the northern Hainan Island and the southern Leizhou Peninsula. Notably, several recently erupted volcanic clusters are situated on the periphery of both anomalies, adding to their significance. Southern Hainan Island, conversely, displays high velocities, particularly within the southern mountainous zone (Figure 1). As the period increases, the two separated anomalies begin to merge. At the period of 10 s, the WSS anomaly becomes more focused, forming a circular shape with a diameter of approximately 1°, while the second anomaly extends northwest towards central Hainan.

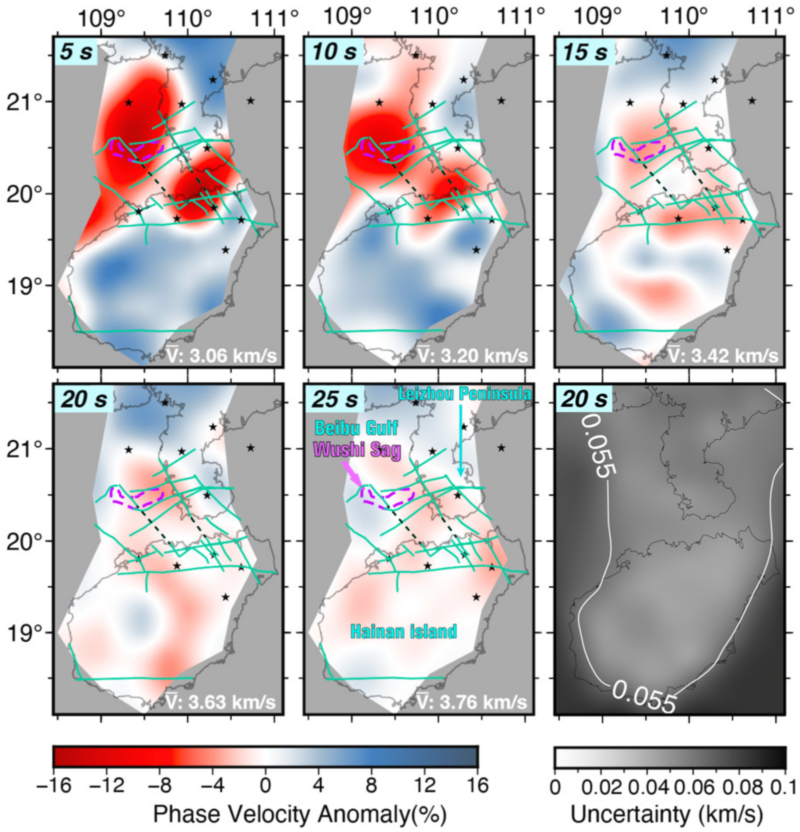

Figure 7. Map view of phase velocity anomaly (dc/c) at five periods, with the mean velocity indicated in the right corner of each panel. Major faults are highlighted in green, while the black dashed lines delineate inferred seafloor faults, extending from those on land. The black stars represent major volcanic clusters. The dashed magenta area highlights the WSS. The bottom-right panel displays the distribution of uncertainties in the inversion at 20 s, represented by the model covariance matrix.

For the periods of 15, 20, and 25 s, which primarily reflect the lower crust and the uppermost mantle structure, the anomaly centered in the WSS beneath the Beibu Gulf remains noticeable, while the one beneath MLVF starts to fade. The distinct anomalies become less defined and attenuate in strength, shifting southward with an increase in the periods.

In addition to these distinct features, the study area exhibits sporadic small high-velocity anomalies in the central Hainan and along the coast, possessing mild strength. These anomalies may be associated with intrusions or metamorphic zones within the otherwise predominantly homogeneous region.

As the phase velocity at each period was inverted independently, it is worth noting that the persistence of the low-velocity WSS anomaly demonstrates robust consistency within the 5–20 s period range, showing a gradual decrease in intensity at longer periods. The reliability of this feature across distinct inversions instills confidence in its authenticity as a genuine geological structure rather than an artifact. Moreover, the spatial correlation of this WSS anomaly with a series of horst and graben structures in the region [61] provides additional structural evidence substantiating the observed velocity reduction.

3.2. Shear Wave Velocity Structure

The absolute shear wave velocities were derived from the Rayleigh wave phase velocities using the method described in Section 2.4. Figure 8 shows horizontal anomaly slices through the 3D shear wave model at six depths ranging from 5 km to 50 km, while four vertical transects are given in Figure 9 (absolute velocity) and Figure S3 (velocity perturbation) in the Supplementary Materials.

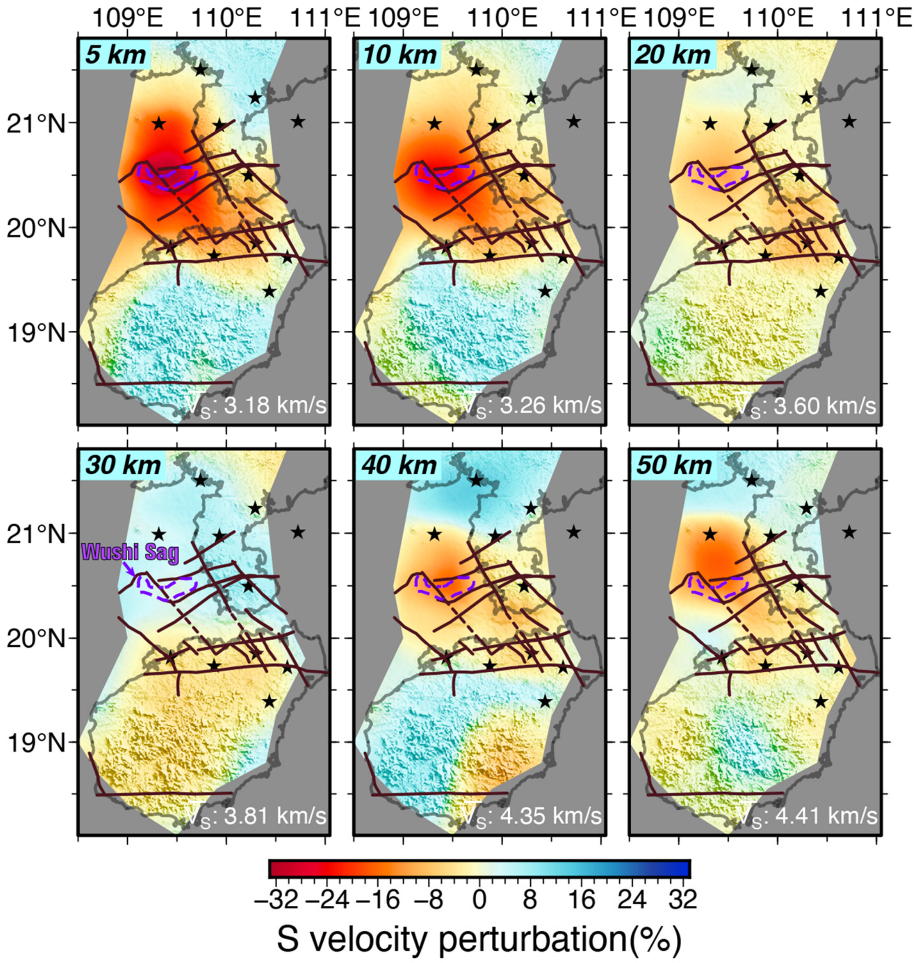

Figure 8. Map views of the S-wave velocity perturbation relative to the mean velocity at various depths. The average velocity used to derive the perturbations is shown in the lower right in each panel. The black stars are volcanic clusters. Major faults are highlighted in black, while the black dashed lines delineate inferred seafloor faults, extending from those on land. The Wushi Sag (WSS) in the Beibu Gulf is delineated by a dashed magenta contour.

The shear wave velocity model generally reflects the primary characteristics of the phase velocity across various periods. At depths of 5 km and 10 km, striking low-velocity anomalies are observed along the eastern Beibu Gulf extending to the Qiongzhou Strait. The maximum −30% anomaly is situated in the Wushi Sag (WSS) at 5 km depth, corresponding to the current igneous zones in the eastern Beibu Gulf, south of the twin islands (Figure 1). With increasing depth, the magnitude and extent of these anomalies diminish. At 20 km, the low-velocity anomaly weakens to approximately −10% but maintains a similar distribution.

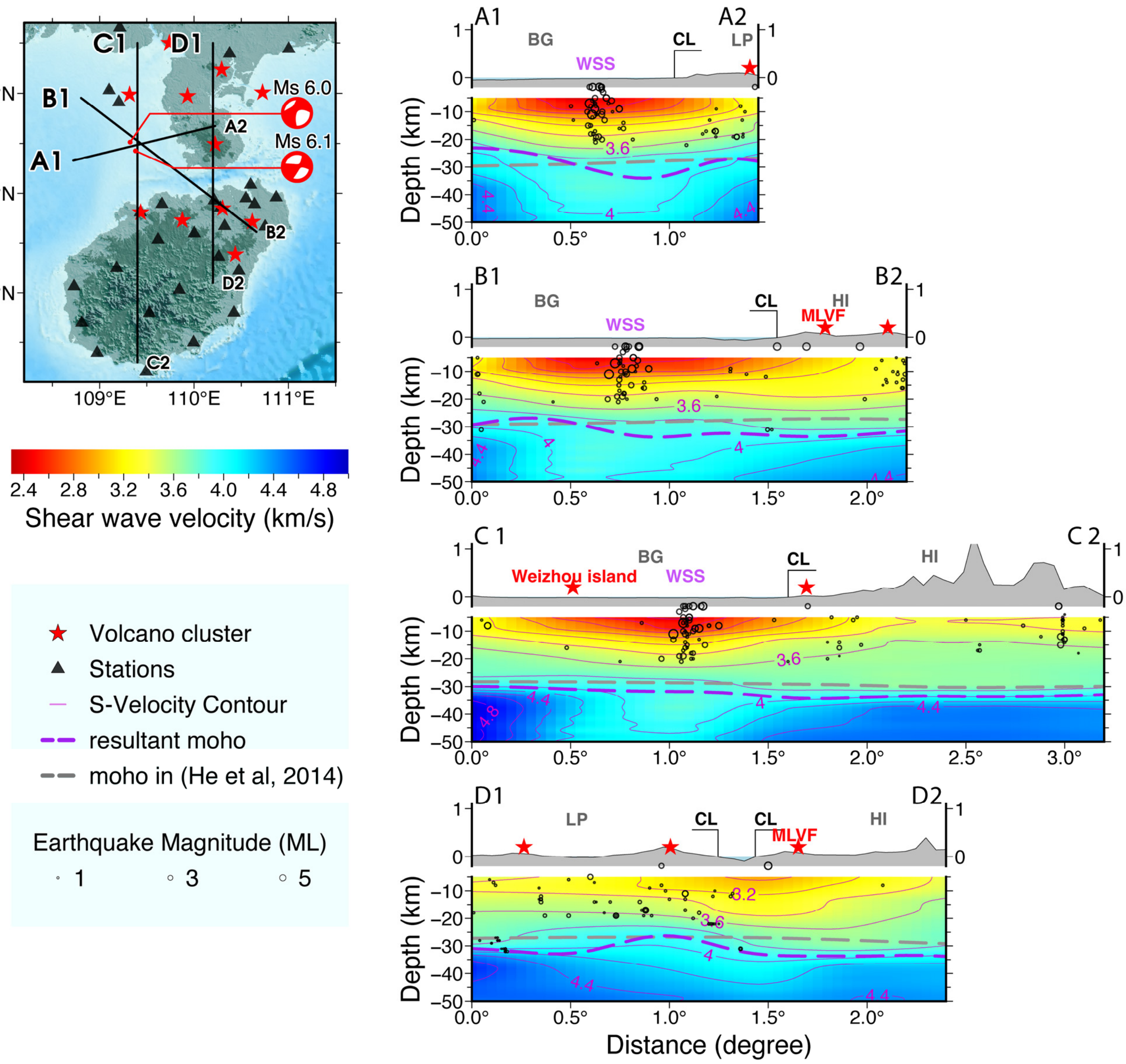

Figure 9. Cross-sections of the derived absolute S-wave velocity model. The locations of the profiles are shown in the topography map on the left. The focal mechanisms of the 31 December 1994 and 10 January 1995 earthquakes in the Wushi Sag (WSS) are also shown. Surface topography along the profile is plotted at the top of each profile, with major geological structures marked and labeled with the following abbreviations: CL: coastline, HI: Hainan Island, LP: Leizhou Peninsula, BG: Beibu Gulf, QS: Qiongzhou Strait, WSS: Wushi Sag, MLVF: Maanling–Leihuling Volcanic Field. Note that the vertical axis of the topography sections is exaggerated. Centers of volcanic clusters (stars) and earthquakes (black circles) within 33 km from the profiles are projected and plotted. Contours with 0.2 km/s velocity interval are also shown by the solid purple lines. The Moho depth from He et al. [36] is shown by the gray dashed line, while the Moho from this study is shown by the purple dashed line.

At around 30 km, which marks the crust–mantle transition zone, there exist lower velocities across almost the whole Hainan Island, with a strength of around −4.5%. This change may be related to the deepening of the Moho beneath the mountainous regions. At depths of 40 and 50 km, prominent low-velocity zones reemerge in the eastern Beibu Gulf, with anomalies of −15%. Another weaker low-velocity body becomes evident in the southeast of Hainan Island.

The vertical transects in Figure 9 provide further insights into the variation in velocity with depth, particularly in relation to volcanism and seismicity. Notably, there is a strong correlation between upper crustal low velocities and volcanic clusters.

Transects A1–A2, B1–B2, and C1–C2 intersect the primary anomaly centered at 20.5° N, 109.4° E (in the WSS) and traverse significant geological structures. A1–A2 passes through the Leizhou Peninsula, B1–B2 intersects the Maanling–Leihuling Volcanic Field (MLVF), and C1–C2 is right next to Weizhou Island and Xieyang Island, extending into the mountainous areas of the western region of Hainan Island in the south. All three transects reveal the lowest velocities in the WSS throughout the upper, mid-crust, and uppermost mantle, super-positioning the nearby seismicity. Notably, the WSS hosts an intense vertical earthquake cluster extending from the shallow crust to at least 25 km depth, unique in the study region (Figures 1 and 9, transects A1–A2, B1–B2, and C1–C2). Section C1–C2 also highlights relatively low velocities beneath Hainan's central mountains. Overall, the three transects highlight the significance of the WSS velocity anomalies in the context of seismicity and the broader region.

Similarly, the north–south section D1–D2 traverses the Leizhou Peninsula, the Qiongzhou Strait, the eastern part of Hainan Island, and the MLVF. This section reveals relatively weak low-velocity anomalies at depths of 0–20 km beneath the MLVF and Qiongzhou Strait relative to ambient velocities. Velocities above 10 km remain below 3.2 km/s. Unlike the previous transects, no distinct pronounced low-velocity anomalies were observed at greater depths.

4. Discussion

4.1. Comparison with Previous Models

Our ambient noise tomographic model exhibits large-scale features consistent with findings from previous regional studies [38,62–64]. These studies identified low-velocity anomalies in a broad area encompassing the Leizhou Peninsula, the eastern Beibu Gulf, and the northernmost part of Hainan Island. Nevertheless, given our significantly smaller study region and denser station coverage (Figure S2 in the Supplementary Materials), our velocity model has brought to light previously unresolved structural details.

Specifically, our results diverge from Huang's [31] teleseismic P- and S-wave tomography placing the most prominent low-velocity anomaly at ~10 km depth below the MLVF in Hainan Island. Instead, our model better aligns with outcomes from the local and teleseismic tomography study by Lei et al. [33], which did not image a strong shallow anomaly below the MLVF. Critically, we imaged two distinct upper crustal low-velocity anomalies in the Beibu Gulf and MLVF, suggesting two separate anomalous structures potentially representing ascending conduits. This in contrast to the previously reported a single centralized anomaly.

Our ambient noise tomography indicates absolute S-wave velocities of approximately 3.4 km/s in the northern Lei–Qiong upper crust. The depth of the inferred Moho discontinuity, marked by the maximum velocity gradient, is around 30 km. These crustal thickness and velocity estimates agree with the regional models of He et al. [36], Liu et al. [38], and Peng et al. [64].

Therefore, while sharing certain broad characteristics with previous large-scale studies, our ambient noise tomography reveals new details, including two distinct upper crustal anomalies and localized velocity estimates validated against broader regional models. The following sections discuss these prominent anomalies and their implications in more depth.

4.2. Predominant Low-Velocity Anomalies

The most striking features in our model are two predominant negative anomalies beneath the Wushi Sag (WSS) in the Beibu Gulf and the Maanling–Leihuling Volcanic Field (MLVF) in northeast Hainan.

The $<-25\%$ maximum velocity reduction in the shallow crust beneath the WSS is significant. However, this ultra-low shear wave velocity is observed globally. For example, beneath the Carpathian–Pannonian region of Central Europe, the <1.8 km/s Rayleigh wave velocities and <2.2 km/s shear wave velocities (anomaly ~ −27%) in Vrancea were observed, and these velocities may be related to the recent volcanism in this region [65]. Under the North Anatolian Fault zone in western Turkey, the <2.5 km/s velocity was found to be associated with sedimentary basins and a fault zone [66]. In addition, the <−30% shear wave velocity anomaly was found in the Tyrrhenian Basin in the Mediterranean region [67] and the Vienna Basin in the Eastern Alps [68]. While the S-wave velocities alone are not conclusive evidence of melt presence, such extreme low velocities strongly imply the existence of partial melts at these depths, as velocities below 3.0 km/s are typically challenging to explain without partial melts [69]. This is further corroborated by evidence from geothermal studies. In the vicinity of the Wushi Sag area within the Beibu Gulf, heat flow values are predominantly higher than the global average of 65 mW/m^2 [70], with the values at a specific probe site being exceptionally elevated, ranging between 90 and 120 mW/m^2 [71]. However, it is worth noting that no recent volcanic activity has been documented in the WSS, suggesting that other contributing factors may be at play in explaining the anomalous wave speeds.

The Wushi Sag is intersected by numerous fault systems [72], a fact evidenced by the frequent seismic activity in the region (see Figure 9). These faults can facilitate the infiltration of fluids, potentially inducing hydrothermal alteration, a phenomenon likely exacerbated by the long-term subaqueous environment that has prevailed since at least the early Miocene [73]. In this context, the circulation of seawater through hot upper crustal rocks can lead to alterations in mineral assemblages, resulting in lower seismic velocities [74]. Cooling due to hydrothermal activities may have prevented the underlying melts from rising and erupting directly in this location. Furthermore, the elevated mantle temperatures originating from deep mantle upwellings may generate volatiles that ascend into the crust, thereby contributing to the velocity reduction [75].

Conversely, the more moderate reduction in velocity observed in the crust of the Maanling–Leihuling Volcanic Field (MLVF) may be explained by residual rocks left behind after the extraction of melt, which generally exhibit not-so-low wave speeds. Similar phenomena have been observed in locations such as Krafla [76], Yellowstone [77], Mt. St. Helens [78], the Cascade Range [79], and various other volcanic regions [4]. The process involves partial melt metasomatism followed by cooling and crystallization, which tends to increase seismic velocities in the residual crust [78]. The MLVF, unlike the WSS, lacks the conditions conducive to hydrothermal fluid penetration.

Therefore, the extreme velocity reductions observed in the WSS crust are likely the result of a combination of factors, including partial melts, fault systems, hydrothermal fluids, and volatiles. The consolidated nature of the crust in the MLVF atop residual high-velocity rocks illustrates the intricate interplay of factors influencing seismic velocities in dynamic hotspot settings.

Similarly, the observed shear wave velocity anomaly of approximately −8% (3.8–3.9 km/s) in the uppermost mantle beneath the WSS cannot be solely attributed to temperature variations and is more plausibly associated with the presence of melt. Previous studies, for example [80–82], have indicated that a reduction of 0.1 km/s in shear wave velocity (Vs) would correspond to an approximate temperature deficit of 200 K in the upper mantle in the absence of melt. While the estimates of melt fraction under a pressure of 10 Kbar, as proposed by Artemieva et al. [81] and Murase [83], may carry some degree of uncertainty, it is reasonable to infer a substantial presence of melt in the uppermost mantle beneath the WSS.

Conversely, in the MLVF (previously considered the center of the Hainan mantle on the crust), where the most recent volcanic activity was documented, there is no clear indication of relatively low velocity in the uppermost mantle (see profile B1–B2 in both Figure 9 and Figure S3 in the Supplementary Materials). Nevertheless, the upper mantle anomaly beneath the WSS seems to be somehow connected to a moderately low-velocity zone in the lower crust beneath the MLVF, as observed in transects B and C in Figures 9 and S3. This connection suggests that the melt reservoir beneath the MLVF may be supplied by melt and volatiles originating from mantle upwellings beneath the WSS.

4.3. Deepened Moho Indicative of Underplating

In the context of geological processes, the Moho boundary, while generally indicative of compositional differences, is also influenced by physical property contrasts that can be modified by various mechanisms such as melting [84]. Typically, the Moho is defined based on an absolute velocity value in tomographic models. However, in the case of this hotspot region, absolute velocities are significantly affected by the elevated temperatures resulting from the deep-seated plume, resulting in the creation of smooth velocity gradients. Consequently, we have defined the Moho as the depth at which the maximum shear wave velocity gradient falls within the range of 3.8–4.1 km/s. This approach takes into account the gradual velocity transitions while still pinpointing the depth at which the most prominent physical property contrast occurs. The resulting Moho is shown in Figure 9.

Our modeled Moho concurs with previous estimates derived from receiver functions and gravity studies [17,19,33,36] and also provides additional insights. Particularly, our model reveals a Moho deepening of approximately 5 km directly beneath the uppermost mantle anomaly in the WSS, which corresponds to the reduced velocities observed in the uppermost mantle. This localized deepening is a strong indicator of underplating, signifying the emplacement of high-density residual mantle melts at the base of the existing crust, likely resulting from the ascent of magma [35,85].

4.4. Conceptual Model for Crust and Magma Interactions Beneath Hainan Hotspot

The central question regarding the magmatism pattern within this hotspot revolves around the location that the rising plume directly impacts, whether that is beneath the currently active MLVF in northern Hainan Island or the WSS.

Previous research assumed that the Hainan plume directly impinged beneath the active MLVF in northeast Hainan [31,42,86]. However, our findings do not reveal a prominent upper mantle low-velocity anomaly beneath the MLVF. Instead, we observed an extreme reduction in velocity in the uppermost mantle beneath the WSS, which implies the presence of significant melt fractions. The lower crustal anomalies beneath the MLVF are relatively subtle, with minor evidence of melt. Most significantly, the lower crustal anomalies are connected to the upper mantle low-velocity region beneath the WSS (see B1–B2 in Figures 9 and 10).

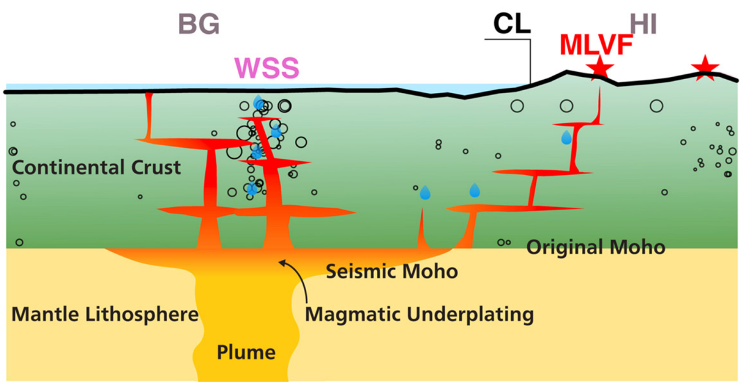

Figure 10. Schematic plot of the proposed magmatic migration model shown along transect B1–B2 in Figure 9 in the Lei–Qiong area. The centers of volcanic clusters (stars) and earthquakes (black circles) within 33 km from the B1–B2 profile are projected and plotted. The blue teardrop-shaped symbols indicate the possible presence of fluids.

This interpretation is supported by the identification of a high-conductivity body in the lower-inclined area westward beneath the MLVF [87]. The shape of this high-conductivity body suggests that the erupted magma did not ascend vertically from a deep source; instead, it rose from depths of 25–30 km to the west, and the magma supply is gradually diminishing.

Additionally, intense vertical earthquake swarms, attributed to magmatic fluids, occur at the WSS location and spatially correspond well with the predominant low-velocity zone [16]. The two most significant recent earthquakes in Lei–Qiong (Ms 6.1 and Ms 6.0) also took place at depths of 20–27 km directly beneath the low-velocity zone in the WSS [18]. The compressional stresses (refer to the focal mechanism in Figure 9) associated with these earthquakes indicate that they are controlled by the WSS fracture zone (refer to the fault pattern Figure 1 and the tectonic background discussed in the Section 1), with fluids, likely reducing friction and generating these deep events [18,88].

Integrating the results and interpretations discussed above, we present a conceptual model in Figure 10 illustrating the inferred crustal and magmatic interactions occurring beneath the Hainan hotspot. The model suggests that the magma originating from the deep mantle beneath the WSS is responsible for the lowest-velocity anomaly in this region. Although the WSS has not experienced recent eruptions, the strength of the low-velocity anomaly indicates the presence of partial melt beneath it. This anomaly could be attributed to long-lasting hydrothermal activities and volatiles released from deep-seated magma. Partial deep-seated magma has migrated to the Leizhou Peninsula and northern Hainan Island, guided by numerous pre-existing crustal faults. Similarly, the volcanic areas on Weizhou Island, Xieyang Island, and the volcanic fields in the Leizhou Peninsula are also directly supplied by this major magma source centered in the WSS, even though they are currently in a post-eruption stage with elevated temperatures.

While this model is primarily based on seismic velocity derived from ambient noise, fully constraining the magmatism pattern for this hotspot requires integrating evidence from other disciplines. A comprehensive marine and terrestrial survey incorporating gravity, magnetic, and geothermal studies would provide additional critical constraints.

5. Conclusions

Ambient noise tomography provides new high-resolution constraints on Hainan plume–crust interactions in the Lei–Qiong region. Beneath the Wushi Sag (WSS) in the Beibu Gulf, extreme upper crustal low velocities correlate with heightened seismicity, indicating the locus of current active magmatism. These anomalies can primarily be attributed to partial melts, hydrothermal alteration, and injected volatiles. Concurrently, the significant low-velocity zone centered in the uppermost mantle of the WSS implies that the Hainan plume is presently impinging on the crust here. Moho deepening suggests plume-related underplating. In contrast, only subtle crustal anomalies have been imaged beneath the Maanling–Leihuling Volcanic Field (MLVF). Rather than a direct plume impact, as previously assumed, we infer that this zone is fed by lateral melt migration from the WSS source, with currently diminished activity following past magmatism.

Supplementary Materials: The following supporting information can be downloaded at: https://www.mdpi.com/article/10.3390/geosciences14030063/s1, Figure S1: normalized azimuthal distribution of noise energy in the 5–30 s period band in the Lei–Qiong region; Figure S2: the ray coverage along the great circle path in the presenting periods; Figure S3: Cross-sections of the derived S-wave velocity perturbation model.

Author Contributions: Conceptualization, M.P. and T.Y.; methodology, M.P., B.M.L., T.Y., Y.D. and H.X.; validation, B.M.L., Y.D. and T.Y.; formal analysis, M.P. and T.Y.; data curation, M.P.; writing—review and editing, M.P., T.Y., B.M.L., T.Y., Y.D. and H.X.; visualization, M.P.; supervision, T.Y.; project administration, H.X.; funding acquisition, T.Y. All authors have read and agreed to the published version of the manuscript.

Funding: This research was funded by the National Natural Science Foundation of China (92058209, 42327804) and Shenzhen Science and Technology Program (KQTD20170810111725321).

Data Availability Statement: The waveform data used in this study were collected from China Earthquake Networks Center and Hainan Seismic Networks, China Earthquake Administration. Data is available at Data Management Centre of China National Seismic Network (SEISDMC; http://www.seisdmc.ac.cn).

Acknowledgments: We thank Jiuchang Hu, Hui Zhang, and Xiangkai Chen at Hainan Earthquake Bureau for providing us with the data. We also thank Zhen Guo for giving us valuable advice. The figures were made using GMT.

Conflicts of Interest: The authors declare no conflicts of interest. The funders had no role in the design of the study; in the collection, analyses, or interpretation of data; in the writing of the manuscript; or in the decision to publish the results.

Appendix A

Table A1. Instrument information for individual stations.

Station Name	Province	Latitude	Longtitude	Sensor	Digitizer
JFL	Hainan	18.6977	108.812	BBVS-60	edas-24IP/edas-GN
WET	Hainan	19.9578	110.87	BBVS-60	edas-24IP/edas-GN
LSH	Hainan	18.4998	109.996	BBVS-60	edas-24IP/edas-GN
LIG	Hainan	19.89	109.66	BBVS-60	edas-24IP/edas-GN
SAY	Hainan	18.204	109.493	BBVS-60	edas-24IP/edas-GN
WZS	Hainan	18.7972	109.528	BBVS-60	edas-24IP/edas-GN
QSL	Hainan	19.6656	110.754	BBVS-60	edas-24IP/edas-GN
CHM	Hainan	19.5968	110.003	BBVS-60	edas-24IP/edas-GN
DOF	Hainan	19.0655	108.729	BBVS-60	edas-24IP/edas-GN
WAN	Hainan	18.8007	110.424	BBVS-60	edas-24IP/edas-GN
YML	Hainan	19.853	110.28	BBVS-60	edas-24IP/edas-GN
SLL	Hainan	19.8082	109.432	BBVS-60	edas-24IP/edas-GN
BSL	Hainan	19.3633	110.262	BBVS-60	edas-24IP/edas-GN
QXL	Hainan	20.0869	110.599	BBVS-60	edas-24IP/edas-GN
JUS	Hainan	18.394	108.974	BBVS-60	edas-24IP/edas-GN
BSH	Hainan	19.248	109.181	BBVS-60	edas-24IP/edas-GN
SHP	Hainan	19.9487	110.55	BBVS-60	edas-24IP/edas-GN
QIH	Hainan	19.2217	110.476	BBVS-60	edas-24IP/edas-GN
QZN	Hainan	19.0291	109.844	CTS-1	EDAS-24IP
NAD	Hainan	19.5337	109.619	BBVS-60	edas-24IP/edas-GN
DAN	Hainan	19.67	110.324	BBVS-60	edas-24IP/edas-GN
HSK	Hainan	19.9285	110.215	BBVS-60	edas-24IP/edas-GN
SAJ	Hainan	19.8887	110.641	BBVS-60	edas-24IP/edas-GN
ZHJ	Gangdong	21.3944	110.376	KS-2000M-60	TDE-324CI
SHD	Gangdong	21.441	111.003	KS-2000M-60	TDE-324CI
YGJ	Gangdong	21.8581	111.954	KS-2000M-60	TDE-324CI
YGD	Gangdong	21.7113	112.245	KS-2000M-60	TDE-324CI
DXS	Guangxi	21.6718	107.947	CMG-3ESPC-60	EDAS-24IP
YLS	Guangxi	22.6351	110.173	?	?
LNS	Guangxi	22.4202	109.281	JCZ-1	EDAS-24L6
BHS	Guangxi	21.6525	109.213	CMG-3ESPC-60	EDAS-24IP
WZD	Guangxi	21.0306	109.101	?	?
XYD	Guangxi	20.9123	109.204	?	?
QZS	Guangxi	22.2764	108.636	?	EDAS-24IP

"?" stands for unknown sensor or digitizer type.

References

1. Zhao, D. Seismic images under 60 hotspots: Search for mantle plumes. *Gondwana Res.* **2007**, *12*, 335–355. [CrossRef]
2. Le, B.M.; Yang, T.; Morgan, J.P. Seismic Constraints on Crustal and Uppermost Mantle Structure Beneath the Hawaiian Swell: Implications for Plume-Lithosphere Interactions. *J. Geophys. Res. Solid Earth* **2022**, *127*, e2021JB023822. [CrossRef]
3. Thompson, R.; Gibson, S.A. Subcontinental mantle plumes, hotspots and pre-existing thinspots. *J. Geol. Soc.* **1991**, *148*, 973–977. [CrossRef]

4. Yang, T.; Shen, Y. P-wave velocity structure of the crust and uppermost mantle beneath Iceland from local earthquake tomography. *Earth Planet. Sci. Lett.* **2005**, *235*, 597–609. [CrossRef]
5. Huang, H.-H.; Lin, F.-C.; Schmandt, B.; Farrell, J.; Smith, R.B.; Tsai, V.C. The Yellowstone magmatic system from the mantle plume to the upper crust. *Science* **2015**, *348*, 773–776. [CrossRef] [PubMed]
6. Ebinger, C.J.; Sleep, N.H. Cenozoic magmatism throughout east Africa resulting from impact of a single plume. *Nature* **1998**, *395*, 788–791. [CrossRef]
7. Waite, G.P.; Smith, R.B. Seismic evidence for fluid migration accompanying subsidence of the Yellowstone caldera. *J. Geophys. Res. Solid Earth* **2002**, *107*, ESE 1-1–ESE 1-15. [CrossRef]
8. Barley, M.E.; Krapez, B.; Groves, D.I.; Kerrich, R. The Late Archaean bonanza: Metallogenic and environmental consequences of the interaction between mantle plumes, lithospheric tectonics and global cyclicity. *Precambrian Res.* **1998**, *91*, 65–90. [CrossRef]
9. Guo, M.; Yu, H.; Hu, J.; Wang, X.; Zheng, Z.; Wang, G. Progress in monitoring and research of activity of volcanoes in northern Hainan Island. *Seismol. Geol.* **2022**, *44*, 1128–1141. [CrossRef]
10. Hu, Y.; Hao, M.; Ji, L.; Song, S. Three-dimensional crustal movement and the activities of earthquakes, volcanoes and faults in Hainan Island, China. *Geod. Geodyn.* **2016**, *7*, 284–294. [CrossRef]
11. Lu, Y.; Wei, Q. Volcano monitoring and research in Qiongbei, Hainan. *J. Coll. Disaster Prev. Tech.* **2005**, *7*, 33–37. (In Chinese) [CrossRef]
12. Huang, Z.; Chai, F. A New Approach to the Quaternary Volcanicity in the Leiqiong Area. *Trop. Geogr.* **1994**, *14*, 1–10.
13. Fan, Q.; Sun, Q.; Sui, J.; Li, N. Trace-element and isotopic geochemistry of volcanic rocks and it's techtonic implications in Weizhou Island and Xieyang Island, Northern Bay. *Acta Petrol. Sin.* **2008**, *24*, 1323–1332.
14. Li, C.; Wang, F.; Zhong, C. Geochemistry of Quaternary basaltic volcanic rocks of Weizhou island in Beihai city of Guangxi and a discussion on characteristics of their source. *Yanshi Kuangwuxue Zazhi (Acta Petrol. Mineralog.)* **2005**, *24*, 1–11. [CrossRef]
15. Li, C.; Wang, F. Holocene volcanic effusion in Weizhou Island and its geological significance. *Miner. Pet.* **2004**, *4*, 28–34. [CrossRef]
16. Lin, J.; Xia, S.; Wang, X.; Zhao, D.; Wang, D. Seismogenic crustal structure affected by the Hainan mantle plume. *Gondwana Res.* **2022**, *103*, 23–36. [CrossRef]
17. Li, Z.; Zhao, W.; Liu, G. A study on deep crust structures and stress situation of the 1605 Qiongshan strong earthquake. *South China J. Seismol.* **2006**, *26*, 28–36. [CrossRef]
18. Zhou, R.-M.; Chen, Y.-T.; Wu, Z.-L. Moment tensor inversion for focal mechanism of the Beibuwan earthquakes. *Acta Seismol. Sin.* **1999**, *12*, 609–617. [CrossRef]
19. Wei, S.S.; Chen, Y.J. Seismic evidence of the Hainan mantle plume by receiver function analysis in southern China. *Geophys. Res. Lett.* **2016**, *43*, 8978–8985. [CrossRef]
20. Xu, X.; Xibing, Y.; Lin, H.U.; Shuicheng, L.; Shixin, F.; Shuai, Z. Characteristics of Fractures in Wushi Sag and Their Influence on Hydrocarbon Accumulation. *Nat. Gas Technol. Econ.* **2016**, *10*, 17–21. [CrossRef]
21. Yan, Q.; Shi, X. Hainan mantle plume and the formation and evolution of the South China Sea. *Geol. J. China Univ.* **2007**, *13*, 311–322. [CrossRef]
22. Yan, P.; Liu, H. Analysis on deep crust sounding results in northern margin of South China Sea. *J. Trop. Oceanogr. (Chin.)* **2002**, *21*, 1–12. [CrossRef]
23. Clift, P.; Lin, J.; Barckhausen, U. Evidence of low flexural rigidity and low viscosity lower continental crust during continental break-up in the South China Sea. *Mar. Pet. Geol.* **2002**, *19*, 951–970. [CrossRef]
24. Clift, P.D.; Sun, Z. The sedimentary and tectonic evolution of the Yinggehai-Song Hong basin and the southern Hainan margin, South China Sea: Implications for Tibetan uplift and monsoon intensification. *J. Geophys. Res.-Solid Earth* **2006**, *111*, B06405. [CrossRef]
25. Sun, Z.; Zhong, Z.; Zhou, D.; Zeng, Z. Continent-ocean interactions along the Red River fault zone, South China Sea. *Cont.-Ocean Interact. East Asian Marg. Seas Geophys. Monogr.* **2004**, *149*, 109–120.
26. Zhang, Y.; Sun, Z.; Zhou, D.; Guo, X.; Shi, X.; Wu, X.; Pang, X. Stretching characteristics and its dynamic significance of the northern continental margin of South China Sea. *Sci. China Ser. D-Earth Sci.* **2008**, *51*, 422–430. [CrossRef]
27. Lebedev, S.; Nolet, G. Upper mantle beneath southeast Asia from S velocity tomography. *J. Geophys. Res.-Solid Earth* **2003**, *108*, 2048. [CrossRef]
28. Lebedev, S.; Chevrot, S.; Nolet, G.; Van der Hilst, R. New seismic evidence for a deep mantle origin of the S. China basalts (the Hainan plume?) and other observations in SE Asia. *Eos Trans. AGU* **2000**, *81*, F1110.
29. Wang, C.; Huang, J. Mantle transition zone structure around Hainan by receiver function analysis. *Chin. J. Geophys.* **2012**, *55*, 1161–1167.
30. Le, B.M.; Yang, T.; Gu, S.Y. Upper mantle and transition zone structure beneath Leizhou-Hainan region: Seismic evidence for a lower-mantle origin of the Hainan plume. *J. Asian Earth Sci.* **2015**, *111*, 580–588. [CrossRef]
31. Huang, J. P- and S-wave tomography of the Hainan and surrounding regions: Insight into the Hainan plume. *Tectonophysics* **2014**, *633*, 176–192. [CrossRef]
32. Huang, J.; Zhao, D. High-resolution mantle tomography of China and surrounding regions. *J. Geophys. Res.-Solid Earth* **2006**, *111*, B09305. [CrossRef]
33. Lei, J.; Zhao, D.; Steinberger, B.; Wu, B.; Shen, F.; Li, Z. New seismic constraints on the upper mantle structure of the Hainan plume. *Phys. Earth Planet. Inter.* **2009**, *173*, 33–50. [CrossRef]

34. Montelli, R.; Nolet, G.; Dahlen, F.A.; Masters, G.; Engdahl, E.R.; Hung, S.H. Finite-frequency tomography reveals a variety of plumes in the mantle. *Science* **2004**, *303*, 338–343. [CrossRef]
35. Wang, X.-C.; Li, Z.-X.; Li, X.-H.; Li, J.; Liu, Y.; Long, W.-G.; Zhou, J.-B.; Wang, F. Temperature, pressure, and composition of the mantle source region of Late Cenozoic basalts in Hainan Island, SE Asia: A consequence of a young thermal mantle plume close to subduction zones? *J. Petrol.* **2012**, *53*, 177–233. [CrossRef]
36. He, R.; Shang, X.; Yu, C.; Zhang, H.; Van der Hilst, R.D. A unified map of Moho depth and Vp/Vs ratio of continental China by receiver function analysis. *Geophys. J. Int.* **2014**, *199*, 1910–1918. [CrossRef]
37. Li, Z.; Lei, J.; Zhao, D.; Wu, B.; Shen, F.; Qiu, X. Three-dimensional P-wave velocity structure of the crust beneath Hainan Island and its adjacent regions, China. *Earthq. Sci.* **2008**, *21*, 441–448. [CrossRef]
38. Liu, H.; Chen, F.; Leng, W.; Zhang, H.J.; Xu, Y.G. Crustal Footprint of the Hainan Plume Beneath Southeast China. *J. Geophys. Res.-Solid Earth* **2018**, *123*, 3065–3079. [CrossRef]
39. Wu, H.-H.; Tsai, Y.-B.; Lee, T.-Y.; Lo, C.-H.; Hsieh, C.-H.; Van Toan, D. 3-D shear wave velocity structure of the crust and upper mantle in South China Sea and its surrounding regions by surface wave dispersion analysis. *Mar. Geophys. Res.* **2004**, *25*, 5–27. [CrossRef]
40. Shen, W.S.; Ritzwoller, M.H.; Kang, D.; Kim, Y.; Lin, F.C.; Ning, J.Y.; Wang, W.T.; Zheng, Y.; Zhou, L.Q. A seismic reference model for the crust and uppermost mantle beneath China from surface wave dispersion. *Geophys. J. Int.* **2016**, *206*, 954–979. [CrossRef]
41. Jia, S.; Li, Z.; Xu, Z.; Shen, F.; Zhao, W.; Yang, Z.; Yang, J.; Lei, W. Crustal structure features of the Leiqiong depression in Hainan Province. *Chin. J. Geophys.-Chin. Ed.* **2006**, *49*, 1385–1394. [CrossRef]
42. Xia, S.; Zhao, D.; Sun, J.; Huang, H. Teleseismic imaging of the mantle beneath southernmost China: New insights into the Hainan plume. *Gondwana Res.* **2016**, *36*, 46–56. [CrossRef]
43. Bensen, G.D.; Ritzwoller, M.H.; Barmin, M.P.; Levshin, A.L.; Lin, F.; Moschetti, M.P.; Shapiro, N.M.; Yang, Y. Processing seismic ambient noise data to obtain reliable broad-band surface wave dispersion measurements. *Geophys. J. Int.* **2007**, *169*, 1239–1260. [CrossRef]
44. Huo, D.; Yang, T. Seismic ambient noise around the South China Sea: Seasonal and spatial variations, and implications for its climate and surface circulation. *Mar. Geophys. Res.* **2013**, *34*, 449–459. [CrossRef]
45. Wang, Y.; Yang, T.; Wu, Y.; Liu, D.; Huang, X.; Wang, J.; Zhong, W.; Shou, H.; Zhou, Y.; Chen, Y. A new broad-band ocean bottom seismograph and characteristics of the seismic ambient noise on the South China Sea seafloor based on its recordings. *Geophys. J. Int.* **2022**, *230*, 684–695. [CrossRef]
46. Xiao, H.; Xue, M.; Pan, M.; Gao, J. Characteristics of microseisms in South China. *Bull. Seismol. Soc. Am.* **2018**, *108*, 2713–2723. [CrossRef]
47. Xiao, H.; Xue, M.; Yang, T.; Liu, C.; Hua, Q.; Xia, S.; Huang, H.; Le, B.M.; Yu, Y.; Huo, D. The characteristics of microseisms in South China Sea: Results from a combined data set of OBSs, broadband land seismic stations, and a global wave height model. *J. Geophys. Res. Solid Earth* **2018**, *123*, 3923–3942. [CrossRef]
48. Yao, H.; Van Der Hilst, R. Analysis of ambient noise energy distribution and phase velocity bias in ambient noise tomography, with application to SE Tibet. *Geophys. J. Int.* **2009**, *179*, 1113–1132. [CrossRef]
49. Froment, B.; Campillo, M.; Roux, P.; Gouédard, P.; Verdel, A.; Weaver, R.L. Estimation of the effect of nonisotropically distributed energy on the apparent arrival time in correlations. *Geophysics* **2010**, *75*, SA85–SA93. [CrossRef]
50. Le, B.M.; Yang, T.; Chen, Y.J.; Yao, H. Correction of OBS clock errors using Scholte waves retrieved from cross-correlating hydrophone recordings. *Geophys. J. Int.* **2017**, *212*, 891–899. [CrossRef]
51. Yao, H.; Gouédard, P.; Collins, J.A.; McGuire, J.J.; van der Hilst, R.D. Structure of young East Pacific Rise lithosphere from ambient noise correlation analysis of fundamental- and higher-mode Scholte-Rayleigh waves. *Comptes Rendus Geosci.* **2011**, *343*, 571–583. [CrossRef]
52. Harmon, N.; Gerstoft, P.; Rychert, C.A.; Abers, G.A.; Salas de la Cruz, M.; Fischer, K.M. Phase velocities from seismic noise using beamforming and cross correlation in Costa Rica and Nicaragua. *Geophys. Res. Lett.* **2008**, *35*, L19303. [CrossRef]
53. Yao, H.; Van Der Hilst, R.D.; Montagner, J.P. Heterogeneity and anisotropy of the lithosphere of SE Tibet from surface wave array tomography. *J. Geophys. Res.-Solid Earth* **2010**, *115*, B12307. [CrossRef]
54. Liu, C.; Yao, H. Surface Wave Tomography with Spatially Varying Smoothing Based on Continuous Model Regionalization. *Pure Appl. Geophys.* **2017**, *174*, 937–953. [CrossRef]
55. Montagner, J. Regional three-dimensional structures using long-period surface waves. *Ann. Geophys* **1986**, *4*, 283–294.
56. Tarantola, A.; Valette, B. Generalized nonlinear inverse problems solved using the least squares criterion. *Rev. Geophys.* **1982**, *20*, 219–232. [CrossRef]
57. Humphreys, E.; Clayton, R.W. Adaptation of Back Projection Tomography to Seismic Travel Time Problems. *J. Geophys. Res.-Solid Earth Planets* **1988**, *93*, 1073–1085. [CrossRef]
58. Zhao, D.; Hasegawa, A.; Horiuchi, S. Tomographic Imaging of P-Wave and S-Wave Velocity Structure beneath Northeastern Japan. *J. Geophys. Res.-Solid Earth* **1992**, *97*, 19909–19928. [CrossRef]
59. Saito, M. DISPER80: A subroutine package for the calculation of seismic normal-mode solutions. In *Seismological Algorithm*; Academic Press: Cambridge, MA, USA, 1988; pp. 293–319.
60. Laske, G.; Ma, Z.; Masters, G.; Pasyanos, M. CRUST 1.0: An updated global model of Earth's crust. *Geophys. Res. Abstr.* **2012**, *14*, 3743. Available online: https://meetingorganizer.copernicus.org/EGU2012/EGU2012-3743-1.pdf (accessed on 13 October 2023).

61. Yang, H.; Liang, J.; Hu, W. Structural features and impacts on hydrocarbon accumulation in Wushi Sag. *J. Southwest Pet. Univ. (Sci. Technol. Ed.)* **2011**, *33*, 41–46. [CrossRef]
62. Lü, J.; Xie, Z.; Zheng, Y.; Zha, X.; Hu, R.; Zeng, X. Rayleigh wave phase velocities of South China block and its adjacent areas. *Sci. China Earth Sci.* **2016**, *59*, 2165–2178. [CrossRef]
63. Zhou, L.; Xie, J.; Shen, W.; Zheng, Y.; Yang, Y.; Shi, H.; Ritzwoller, M.H. The structure of the crust and uppermost mantle beneath South China from ambient noise and earthquake tomography. *Geophys. J. Int.* **2012**, *189*, 1565–1583. [CrossRef]
64. Peng, J.; Huang, J.L.; Liu, Z.K.; Xing, K. Constraints on S-wave velocity structures of the lithosphere in mainland China from broadband ambient noise tomography. *Phys. Earth Planet. Inter.* **2020**, *299*, 106406. [CrossRef]
65. Ren, Y.; Stuart, G.; Houseman, G.; Grecu, B.; Hegedüs, E.; Dando, B.; Lorinczi, P.; Gogus, O.; Kovács, A.; Torok, I.; et al. Crustal structure of the carpathian-pannonian region from ambient noise tomography. *Geophys. J. Int.* **2013**, *195*, 1351–1369. [CrossRef]
66. Taylor, G.; Rost, S.; Houseman, G.A.; Hillers, G. Near-surface structure of the North Anatolian Fault zone from Rayleigh and Love wave tomography using ambient seismic noise. *Solid Earth* **2019**, *10*, 363–378. [CrossRef]
67. Manu-Marfo, D.; Aoudia, A.; Pachhai, S.; Kherchouche, R. 3D shear wave velocity model of the crust and uppermost mantle beneath the Tyrrhenian basin and margins. *Sci. Rep.* **2019**, *9*, 3609. [CrossRef] [PubMed]
68. Szanyi, G.; Gráczer, Z.; Balázs, B.; Kovacs, I. The transition zone between the Eastern Alps and the Pannonian basin imaged by ambient noise tomography. *Tectonophysics* **2021**, *805*, 228770. [CrossRef]
69. Eberhart-Phillips, D.; Stanley, W.D.; Rodriguez, B.D.; Lutter, W.J. Surface seismic and electrical methods to detect fluids related to faulting. *J. Geophys. Res. Solid Earth* **1995**, *100*, 12919–12936. [CrossRef]
70. Davies, J.H. Global map of solid Earth surface heat flow. *Geochem. Geophys. Geosystems* **2013**, *14*, 4608–4622. [CrossRef]
71. Yu, L.; Zhang, J.; Chen, S.; Dong, M.; Xu, C. Thermal-gravity equilibrium adjustment mechanism of Zhenbei-Huangyan seamount chain. *Acta Seismol. Sin.* **2015**, *37*, 565–574.
72. Dong, F.; Wu, K.; Cui, L.; Li, Y.; Zhou, P.; Dong, W. Identification and characteristics of structural transfer zones in the east area of Wushi Sag, Beibuwan Basin. *Oil Geophys. Prospect.* **2021**, *56*, 1180–1189. [CrossRef]
73. Liang, G. A study of the genesis of Hainan Island. *Geol. China* **2018**, *45*, 693–705. [CrossRef]
74. Zhao, G.; Unsworth, M.J.; Zhan, Y.; Wang, L.; Chen, X.; Jones, A.G.; Tang, J.; Xiao, Q.; Wang, J.; Cai, J.; et al. Crustal structure and rheology of the Longmenshan and Wenchuan Mw 7.9 earthquake epicentral area from magnetotelluric data. *Geology* **2012**, *40*, 1139–1142. [CrossRef]
75. Julian, B.R.; Miller, A.D.; Foulger, G.R. Non-double-couple earthquakes 1. Theory. *Rev. Geophys.* **1998**, *36*, 525–549. [CrossRef]
76. Brandsdóttir, B.; Menke, W.; Einarsson, P.; White, R.S.; Staples, R.K. Färoe-Iceland Ridge Experiment 2. Crustal structure of the Krafla central volcano. *J. Geophys. Res. Solid Earth* **1997**, *102*, 7867–7886. [CrossRef]
77. Benz, H.M.; Smith, R.B. Simultaneous inversion for lateral velocity variations and hypocenters in the Yellowstone Region using earthquake and refraction data. *J. Geophys. Res. Solid Earth* **1984**, *89*, 1208–1220. [CrossRef]
78. Lees, J.M.; Crosson, R.S. Tomographic inversion for three-dimensional velocity structure at Mount St. Helens using earthquake data. *J. Geophys. Res. Solid Earth* **1989**, *94*, 5716–5728. [CrossRef]
79. Evans, J.R.; Zucca, J.J. Active high-resolution seismic tomography of compressional wave velocity and attenuation structure at Medicine Lake Volcano, Northern California Cascade Range. *J. Geophys. Res. Solid Earth* **1988**, *93*, 15016–15036. [CrossRef]
80. Anderson, O.L.; Isaak, D.; Oda, H. High-temperature elastic constant data on minerals relevant to geophysics. *Rev. Geophys.* **1992**, *30*, 57–90. [CrossRef]
81. Artemieva, I.M.; Billien, M.; Lévêque, J.-J.; Mooney, W.D. Shear wave velocity, seismic attenuation, and thermal structure of the continental upper mantle. *Geophys. J. Int.* **2004**, *157*, 607–628. [CrossRef]
82. Takei, Y. Effects of partial melting on seismic velocity and attenuation: A new insight from experiments. *Annu. Rev. Earth Planet. Sci.* **2017**, *45*, 447–470. [CrossRef]
83. Murase, T. Shear wave velocity in partially molten peridotite at high pressure. *Year Book Carnegie Inst. Wash.* **1980**, *79*, 307–310.
84. Mengel, K.; Kern, H. Evolution of the petrological and seismic Moho-implications for the continental crust-mantle boundary. *Terra Nova* **1992**, *4*, 109–116. [CrossRef]
85. Thybo, H.; Artemieva, I.M. Moho and magmatic underplating in continental lithosphere. *Tectonophysics* **2013**, *609*, 605–619. [CrossRef]
86. Wei, F.; Wei, W.; Yu, H. The Cenozoic volcanic fields in northern Hainan Island and Leizhou Peninsula, South China: Eruption history, magma source and dynamic background. *Geol. Soc. Lond. Spec. Publ.* **2020**, *510*, 179–196. [CrossRef]
87. Sun, X.; Zhan, Y.; Zhao, G.; Zhao, l.; Deng, Y.; Hu, Y.; Hu, J.; Xiang, X. Three-dimensional magnetotelluric imaging of the deep magmatic system beneath Maanling-Leihuling volcanic cluster area in northeast Hainan Province. *Seismol. Geol.* **2020**, *42*, 14. [CrossRef]
88. Reyners, M.; Eberhart-Phillips, D.; Stuart, G. The role of fluids in lower-crustal earthquakes near continental rifts. *Nature* **2007**, *446*, 1075–1078. [CrossRef]